


# Dynamics of the Water Hydrogen Bond Network at Ionic, Nonionic, and Hydrophobic Interfaces in Nanopores and Reverse Micelles

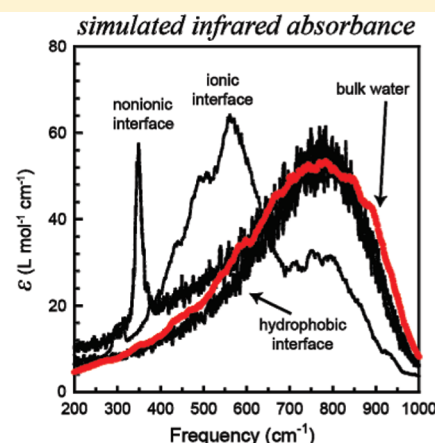
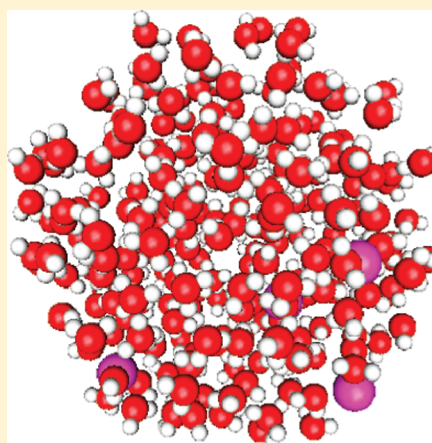
Daniel E. Rosenfeld<sup>\*,†</sup> and Charles A. Schmuttenmaer<sup>\*</sup>

Department of Chemistry, Yale University, 225 Prospect Street, P.O. Box 208107, New Haven, Connecticut 06520-8107, United States

 Supporting Information

**ABSTRACT:** The effects of water confinement on hydrogen bond dynamics and hydrogen bond exchange have been analyzed by molecular dynamics simulations for a series of different sizes of spherical nanopores of ionic, nonionic, and hydrophobic interfaces. We have calculated translational diffusion residence times, orientational decay time constants, the infrared spectra, correlation functions describing the hydrogen bond network, the hydrogen bond exchange time and rate constant, and ensemble

averages of the hydrogen bond exchange reaction coordinate. We focus on the interfacial layer and bulklike interior of these small water containing nanostructures. Our results indicate a universal slowdown in rotational and hydrogen bond dynamics at the interface relative to bulk water. The interiors of nanopores with highly charged interfaces undergo qualitatively different dynamics than those in other nanopores. The rotational jump hydrogen bond exchange mechanism is shown to be robust and universal, even for this variety of interfaces. The implications of these results are discussed in terms of the role of confinement vs interface structure on water dynamics in nanopores.



## 1. INTRODUCTION

Bulk liquids have been observed and characterized over the past several decades. Recently, focus has shifted to liquids involving solutes and complex structures such as micelles or reverse micelles. Water confined within such nanoscopic microemulsions has been shown to have different dynamics from the bulk. These changes to water structure and dynamics upon confinement are important due to the range of physical systems which exhibit a confined geometry. Examples include reverse micelles, nanoporous glasses, clays, zeolites, and proteins. An ideal model system for confined liquids is a reverse micelle (RM). A RM forms when a surfactant with a hydrophilic head group and a hydrophobic tail forms a microemulsion of water in a nonpolar liquid. A commonly studied system is the AOT/water/isooctane system. Water confined within such a nanopore experiences significant perturbations to its structure and dynamics. The AOT/water/isooctane system has been extensively studied both experimentally and theoretically.<sup>1–17</sup>

In this article, we study three different types of nanopores to determine the importance of the type of interface upon confinement of water. We have previously performed simulations of AOT/water/isooctane, a RM system which exhibits a highly charged ionic interface.<sup>17</sup> We extend our previous work by comparing the

dynamical perturbations of a hydrophilic nonionic (NI) interface in a nanopore and a hydrophobic interface in a nanopore to that found in the previous simulations. We focus on perturbations to orientational dynamics, hydrogen bond dynamics, and librational dynamics. Comparison of trends in librational and hydrogen bond dynamics allows us to examine the influence of both transient and long-time perturbations to the time evolution of the water hydrogen bond network.

The AOT/water/isooctane system has been rigorously studied by many experimental techniques, and several theoretical models have been investigated by MD simulations.<sup>1–17</sup> Previous work has shown large slowdowns in dynamics at the interface, radial stratification of water, and changes in water structure through the hydrogen bond network in the layers of water nearest to the interface.<sup>11,12</sup> Experimental and theoretical work have shown slowdowns in diffusion in the RMs, and have investigated the effects of counterion exchange on all of the above properties.<sup>11,13,14</sup> Our previous work focused on calculating the IR absorbance

**Received:** October 7, 2010

**Revised:** December 4, 2010

**Published:** December 23, 2010

spectrum between 400 and 1000  $\text{cm}^{-1}$  in order to replicate experimental data from the same spectral range.<sup>17,18</sup> We determined that the characteristic red shift and isosbestic phenomenology in the spectra were due to multiple subensembles of water absorbing at different frequencies. The water at the trapped layer experienced the strongest perturbation and underwent librational motion at significantly red-shifted frequencies.<sup>17</sup> This motion is governed by the local potential energy surface, and these transient dynamics are thus highly sensitive to local changes in structure and hydrogen bonding.

The long-time behavior of the hydrogen bond network in these systems has not yet been presented in a way meant for comparison to other systems. Many other workers are interested in reproducing experimental properties of reverse micelles and nanoconfined water, yet none have looked at dynamics at readily comparable interfacial structures in an effort to determine the general behavior of interfaces. Some efforts have reproduced experimental dynamic quantities (orientational relaxation and spectral diffusion) in AOT reverse micelles.<sup>19,20</sup> Other efforts have looked at static quantities at a continuously tuned interface (from nonpolar to polar).<sup>21</sup> As successful as these efforts are, they are not capable of addressing the counterfactual questions which must be addressed to tease out the general trends. Specifically, given an AOT-like interface that is not ionic, what would the dynamics be? Answering this question can lead us to general rules for how such aqueous interfaces behave.

Water at other hydrophilic and hydrophobic interfaces has been studied extensively in the literature both experimentally and theoretically.<sup>16,22–30</sup> Common results are that translational diffusion is augmented at hydrophobic interfaces and that the hydrogen bond network slows down at both types of interfaces.<sup>25,27,28,31–35</sup> Furthermore, hydrogen bonds are stronger at hydrophobic interfaces evidenced by the less than proportional decrease in hydrogen bonding despite a large decrease in nearest-neighbor density.<sup>9,36</sup> Although these interfaces have been interesting to other workers for some time, there has not yet been a comparative study between ionic, NI hydrophilic, and hydrophobic interfaces in a confined nanopore. Understanding the differences in perturbations to water confined at these interfaces is important for understanding confinement of liquids in general. We seek to determine the factors which lead to specific changes to water dynamics in confined environments. We also clearly separate the effects of transient and long-time dynamical perturbations.

Hydrogen bond dynamics have previously been investigated theoretically in bulk and nonbulk systems by calculating correlation functions which describe the structural relaxation of the hydrogen bond network and lifetime of a hydrogen bond.<sup>25,37–41</sup> The long-time structural dynamics are typically understood to be dominated by the diffusive characteristics of the system, and the short-time hydrogen bond breaking is dominated by the number of nearest neighbors and bond energies.<sup>25</sup> Results from these calculations have shown that water in an ionic atmosphere undergoes slower structural relaxation due to drag from the ions which causes slower diffusion of water molecules, and also that it has weakened hydrogen bonding and shorter hydrogen bond lifetimes due to the electric field of the ions.<sup>40</sup> Water near an air–water interface has been shown to undergo slower structural relaxation than bulk despite faster diffusion. This is attributed to the increased strength of hydrogen bonds at the interface, which cause less frequent breaking of hydrogen bonds.<sup>25,37</sup> Hydrogen bond dynamics have also been investigated at micellar interfaces, and the hydrogen bond networks demonstrate significantly

slower relaxation at such interfaces.<sup>33,42</sup> Furthermore, water–surfactant and water–water hydrogen bond dynamics have been studied for AOT adsorbed at the air–water interface. Results from these MD simulations have shown strong water–surfactant hydrogen bonds and a structural rigidity within the first hydration layer of AOT characterized by slower hydrogen bond dynamics.<sup>41</sup>

Molecular dynamics simulations have suggested that the water hydrogen bond network evolves through concerted rotational jumps.<sup>43,44</sup> This mechanism has been most strongly elucidated by calculations from simple molecular dynamics simulations of bulk water. In this mechanism, water initially hydrogen bonded to another water molecule inside its first hydration shell rotates about 60° in a subpicosecond jump to form a hydrogen bond with a nearby water in its second hydration shell. The orientational dynamics implied by the rotational jump mechanism agree well with the dynamics that have been measured experimentally through ultrafast spectroscopy. The mechanism and rate of hydrogen bond exchange has been shown to be invariant with respect to hydrogen bond strength due to the dependence on the availability of a new hydrogen-bonding partner, which does not depend on the original strength of the bond.<sup>43</sup> We seek to determine whether this mechanism is robust and common to heterogeneous systems containing water. We therefore investigate this mechanism for water in the presence of complex interfaces and nanoconfined environments. We elucidate the hydrogen bond exchange mechanism in ionic, NI, and hydrophobic nanopores through the same methods used by Laage and Hynes.<sup>43,44</sup>

We apply the above methods to study hydrogen bond networks and exchange to confined water at ionic, NI, and hydrophobic interfaces. We compare the trends across interface types and extract commonalities and differences to help determine the fundamentally important features of interfaces which can impact water dynamics.

## 2. COMPUTATIONAL METHODS

**2.1. Model Details.** The model for AOT/water/isooctane has been previously described in great detail, and we therefore provide only a brief sketch of its primary characteristics.<sup>9–14,17</sup> The RMs consist of unified atom head groups confined to a spherical surface, sodium counterions, and SPC/E water molecules trapped within the sphere. The head groups are constrained to the spherical surface by a radial harmonic potential function. The molecular volumes are based on experimental density data for water and hard-sphere radii for the ions and head groups as reported previously in the literature.<sup>9–14,17</sup> The radii of the RMs are calculated after linear interpolation of light scattering data as a function of the number of surfactant molecules at a particular  $w_0$  (where  $w_0 = [\text{water}]/[\text{surfactant}]$ ).<sup>9,45</sup> A wall potential which prevents water molecules from exiting the spherical cage of head groups is also included in the model. The wall potential is obtained by integrating a continuum of Lennard-Jones sites on a spherical surface.<sup>9</sup> Recently, this model has been updated by Ladanyi<sup>20</sup> (and subsequently used by Skinner<sup>19</sup>) to include fully atomistic AOT molecules and a fully atomistic solvent. Studies of the dynamics affecting the OH vibrational stretch line shape in the atomistic vs reduced model have suggested that the reduced model induces too much order in the interfacial layer.<sup>19</sup> Due to the simplified approach in this article, the reduced model is sufficient to show the differences among the different types of interfaces.

The model for the NI hydrophilic nanopores is similar to the model for ionic RMs described above. Instead of head groups and counterions, there are solely NI head groups. These head groups

**Table 1. Numbers of Molecules and Dimensions for the Various Simulations Performed**

	$n_{\text{water}}$	$n_{\text{HG}}$	$R$ (Å)	$d_{\text{int}}$ (Å)
$w_0 = 1$ (AOT)	21	21	10.25	5.33
$w_0 = 2$ (AOT)	52	26	11.40	5.03
$w_0 = 3$ (AOT)	96	32	13.25	4.90
$w_0 = 4$ (AOT)	140	35	14.10	4.79
$w_0 = 7.5$ (AOT)	525	70	19.40	4.58
$w_0 = 10$ (AOT)	980	98	22.90	4.63
$w_0 = 1$ (NI)	42	42	10.25	4.94
$w_0 = 2$ (NI)	82	41	11.40	5.23
$w_0 = 3$ (NI)	144	48	13.25	5.30
$w_0 = 4$ (NI)	192	48	14.10	5.52
$w_0 = 7.5$ (NI)	630	84	19.40	5.57
$w_0 = 10$ (NI)	1120	112	22.90	5.60
HC1	65	—	10.25	3.06
HC2	105	—	11.40	3.14
HC3	169	—	13.25	3.10
HC4	218	—	14.10	3.10
HC7.5	674	—	19.40	3.15
HC10	1185	—	22.90	3.18

consist of a unified atom  $\text{CH}_2$  site and an atomistic OH with a  $108.5^\circ$  COH bond angle. The C—O bond length is  $1.430$  Å and the O—H bond length is  $0.945$  Å. These parameters were taken from the OPLS set of parameters<sup>46</sup> which have been previously used in simulations of NI surfactants and water.<sup>47</sup> The NI head groups were evenly spaced upon a spherical surface and constrained by two harmonic potentials. The first harmonic potential is the same as the one in the AOT case, a radial harmonic potential which preserves the spherical shape of the nanopore. The second harmonic potential acts in the plane tangent to the sphere at the original point of head group placement. This second potential prevents the entire nanopore from rotating. The potential was tuned to be the weakest possible yet still preserving zero net angular momentum throughout the entire trajectory. This measure was necessary due to numerical inaccuracy of the rotational leapfrog algorithm previously studied by the originator of the method.<sup>48</sup>

In order to generate NI nanopores which are comparable to the ionic RMs, we constrained the nanopores to have the same radii and  $w_0$  values as the RMs. Since there is no experimental data to generate the proper number of head groups, we varied the number of head groups in a set of test  $w_0 = 4$  simulations until the interior water density was as close to bulk as possible within the constraint of integral number of head groups. These simulations then allowed us to calculate the volume of the NI head group which penetrates beyond the radial harmonic potential which acts upon the center of mass of the head group ( $16.21$  Å<sup>3</sup> per molecule). The rest of the parameters for the nanopore simulations were calculated using this molecular volume.

The hydrophobic cavities (HCs) consisted of only the wall potential and confined water molecules. The number of water molecules was calculated by subtracting the  $\sigma_{\text{wall}}$  parameter from the radius of the HC and calculating the number of water molecules which will fill this smaller spherical space. By subtracting the zero-crossing distance of the wall potential ( $2.5$  Å), a molecular volume of  $\sim 30$  Å<sup>3</sup> for water is realized. This ensures that the HC results will be

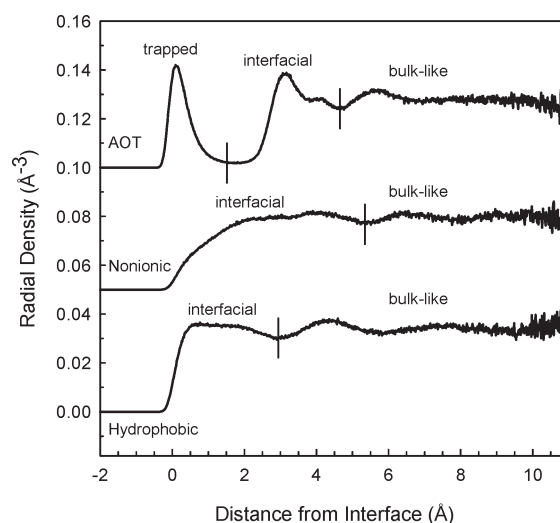


**Figure 1.** Radial density of oxygen atoms in AOT (ionic), nonionic, and hydrophobic nanopores. The vertical lines denote the cutoffs for interfacial versus bulklike water. For the ionic head groups, an additional trapped region is present. A distance value of zero corresponds to the zero-crossing point of the wall potential for all nanopores, which is also the minimum of the harmonic potential for the ionic and non-ionic nanopores. For a discussion of how the regions are used in the analysis, see text.

comparable with both the ionic RM and NI nanopore results, since all the simulations will consist of water confined on the same length scale.

The set of nanopore sizes, including number of water molecules and head groups simulated, is reported in Table 1.

**2.2. Simulation Details.** The molecules in the simulations were rigid, and the translational and rotational degrees of freedom were separated. For water the SPC/E model was used.<sup>49</sup> The translational equations of motion were integrated using the leapfrog version of the Verlet algorithm.<sup>50</sup> The rotational coordinates for the rigid molecules were represented by quaternions and a modified leapfrog integration algorithm was applied.<sup>48,50</sup> A 2 fs time step was used for both integration algorithms throughout all simulations. A Berendsen thermostat was used for all simulations for thermal averaging.<sup>51</sup> For equilibration periods the time constant was 1.0 ps and for averaging periods the time constant was 2.0 ps.

Equilibration consisted of a period during which the simulation volume was shrunk in order to generate a valid starting configuration, followed by a 100 ps trajectory at 500 K, a linear descent to 298.2 K over 50 ps, and finally a 200 ps equilibration period at 298.2 K. The averaging period after equilibration was 2 ns.

The bulk water simulation consisted of 216 SPC/E water molecules incorporating periodic boundary conditions simulated using the same methods described above. The Ewald sum method was used for the long-range interactions.<sup>50</sup> All simulation and data analysis code was developed by the authors.

The nanopore simulations were separated into different regions based upon the radial density profile. For the NI nanopores and HCs we identify a cutoff distance  $d_{\text{int}}$  ( $d$  being the distance from the interface) which is the first minimum in the radial density after the first peak in the radial density profile. For the AOT RMs the interfacial cutoff distance is the location of third minimum in the radial density. Water farther from the interface than  $d_{\text{int}}$  is defined as bulklike. For NI nanopores and HCs water closer to the interface than  $d_{\text{int}}$  is called interfacial, and for AOT RMs water farther than  $1.5$  Å yet closer than  $d_{\text{int}}$  is called bound. Figure 1 shows how the regions are generated from the oxygen



radial density profile for nanopores of size  $w_0 = 4$ , and their values are reported in Table 1. For the remainder of the paper, we focus on bulklike water and the bound and interfacial water in the confined systems since these water species are the most similar to each other and will illustrate the contrast between the different interface types studied here. The trapped water in AOT RMs has incredibly slow translational and orientational dynamics as has been previously shown.<sup>9</sup> Also these water molecules rarely hydrogen bond with other water molecules, and water in the hydration layer of AOT has very slow hydrogen bond dynamics<sup>41</sup> (a result we have replicated but do not focus on here).

**2.3. Frequency-Dependent Dielectric Permittivity.** We previously found that for classical rigid body simulations of water the most appropriate methodology for calculating the frequency-dependent dielectric permittivity is that of Caillol and co-workers.<sup>17</sup> This method reflects the proper boundary conditions for RM and nanopore systems and also allows for the inclusion of mobile ions.<sup>52</sup> A complete description may be found in ref 17, and we note that this method is numerically equivalent to the best quantum-corrected classical approach (that being a harmonic correction factor to the quantum mechanical expression) for the calculation of IR spectra from MD simulations, but is itself not quantum corrected.<sup>53,54</sup> For a direct comparison for the case of bulk water please see the Supporting Information of ref 17. Below we summarize the important relations and equations.

For the following set of relations, we define the complex generalized dielectric permittivity, which includes dispersion and absorption due to both dielectric and conductive phenomena, as

$$\eta(\omega) = \varepsilon(\omega) + \frac{4\pi i \sigma(\omega)}{\omega} \quad (1)$$

where  $\varepsilon(\omega)$  is the frequency-dependent complex relative dielectric permittivity and  $\sigma(\omega)$  is the complex conductivity. The following relationships are used to calculate  $\varepsilon(\omega)$  and  $\sigma(\omega)$ :

$$\left[ \frac{2\Sigma^*(\omega) + 3}{2\Sigma^*(\omega) + 3 + \Sigma(\omega)} \right] \frac{\varepsilon(\omega) - 1}{4\pi} = \frac{\beta}{3V} \left[ \langle \mathbf{M}_W^2 \rangle + i\omega \int_0^\infty \langle \mathbf{M}_W(t) \cdot \mathbf{M}_W(0) \rangle e^{i\omega t} dt + \int_0^\infty \langle \mathbf{M}_W(t) \cdot \mathbf{J}_I(0) \rangle e^{i\omega t} dt \right] \quad (2)$$

$$\left[ \frac{2\Sigma^*(\omega) + 3}{2\Sigma^*(\omega) + 3 + \Sigma(\omega)} \right] \sigma(\omega) = \frac{\beta}{3V} \left[ \int_0^\infty \langle \mathbf{J}_I(t) \cdot \mathbf{J}_I(0) \rangle e^{i\omega t} dt + i\omega \int_0^\infty \langle \mathbf{J}_I(t) \cdot \mathbf{M}_W(0) \rangle e^{i\omega t} dt \right] \quad (3)$$

where  $\Sigma(\omega) = \eta(\omega) - 1$ , and

$$\mathbf{M}_W(t) = \sum_i \mathbf{m}_i(t) \quad (4)$$

$$\mathbf{J}_I(t) = \sum_j q_j \mathbf{v}_j(t) \quad (5)$$

where  $i$  and  $j$  are sums over the dipolar molecules and ions respectively, and the asterisk (\*) denotes the properties of the dielectric continuum. We note that the functions  $\Sigma^*$  and  $\Sigma$  are the

electric susceptibilities of the solvent and the system respectively within a factor of  $4\pi$ ; these factors arise in the solution of the field equations for the system and we refer the reader to ref 17 for additional details. For a periodic simulation, the relations remain the same except that the fractions containing  $\Sigma^*$  and  $\Sigma$  in front of  $\varepsilon(\omega)$  and  $\sigma(\omega)$  in eqs 2 and 3 are equal to 1. The complex refractive index,  $\hat{n}(\omega) = n(\omega) + ik(\omega)$ , is the square root of the generalized complex dielectric permittivity [ $\eta(\omega)$  in eq 1]. The frequency-dependent absorption coefficient is obtained from the imaginary part of the complex index of refraction,  $k(\omega)$ , using  $\alpha(\omega) = 2\omega k(\omega)/c$ , where  $c$  is the speed of light in vacuum. The absorbance spectra have been scaled by the concentration of the water in the RM to yield the molar absorption coefficient,  $\varepsilon$ , of the water molecules (not to be confused with the permittivity). For a nonperiodic spherical system which does not contain ions, the absorbance is calculated as above except that  $\mathbf{J}_I(t) = 0$ .

For a *periodic* simulation of bulk water where there are no mobile ions, the complex permittivity is given by the relation

$$\frac{\varepsilon(\omega) - 1}{4\pi} = \frac{\beta}{3V} \left[ \langle \mathbf{M}_W^2 \rangle + i\omega \int_0^\infty \langle \mathbf{M}_W(t) \cdot \mathbf{M}_W(0) \rangle e^{i\omega t} dt \right] \quad (6)$$

**2.4. Translational Mobility.** To characterize the translational mobility of water confined in ionic, NI, and hydrophobic RMs, we calculate the ensemble averaged mean-squared displacement (MSD) as a function of time. In bulk solution this calculation results in plots which are linear at long times and allows estimation of the diffusion coefficient. However, in confined and nonhomogenous systems the assumptions which lead to the standard Einstein relation and the Green–Kubo relation do not hold. There is a general method for calculating diffusion coefficients in confined and non-homogenous systems,<sup>55</sup> but the estimation is nontrivial and beyond the scope necessary for investigating the trends in translational mobility in these systems. Therefore, the ensemble average mean-squared displacement is calculated for 15 ps from MD trajectory data for different regions of the RMs. The mobilities may be compared through the water's mean translational residence time for each region and the total system. The residence time,  $t_{\text{res}}$ , is the time it takes for the water to translate its own diameter ( $\sim 3 \text{ \AA}$ ). The times were calculated by fitting the MSD to a power law ( $t^\alpha$ ;  $0 < \alpha < 1$ ) to accurately determine when the MSD was equal to  $9 \text{ \AA}^2$  (which corresponds to translation by one water diameter).<sup>56</sup>

**2.5. Orientational Dynamics.** The orientational dynamics of water in the different nanopores is investigated by calculation of the single molecule dipole moment autocorrelation function:

$$\langle e^{\hat{\mu}}(0) \cdot e^{\hat{\mu}}(t) \rangle = \frac{\langle \vec{\mu}(0) \cdot \vec{\mu}(t) \rangle}{\langle |\mu|^2 \rangle} \quad (7)$$

where  $e^{\hat{\mu}}$  is the unit vector in the direction of dipole  $\vec{\mu}$ . We calculate the single dipole autocorrelation functions for different regions of nanoconfined water in ionic, NI, and hydrophobic RMs over a 25 ps interval. Regional water is defined as water which is within a region at time zero. The orientational correlation functions for water in NI and hydrophobic cavities have tails which are robustly fit by single exponentials beginning at 2 ps (adjusted  $R^2$  is  $>0.99$  for all cases; see Figure S1 in the Supporting Information for a typical example). The orientational relaxation time  $\tau_1^{\hat{\mu}}$  is calculated by numerical integration from zero to 2 ps to avoid difficulties fitting the fast librational oscillation and decay, followed by analytical integration of the

best fit exponential tail. The relaxation time  $\tau_1^{\hat{\mu}}$  is therefore defined as

$$\tau_1^{\hat{\mu}} = \int_0^{+\infty} \langle \hat{\mu}(0) \cdot \hat{\mu}(t) \rangle dt \quad (8)$$

Since the single dipole autocorrelation functions for the ionic RMs are nonexponential, extraction of the relaxation time does not work with the simple method above. Therefore, we only report the relaxation times for the sizes  $w_0 = 4, 7.5$ , and 10 and compare the relative slowdown with the NI nanopore and HC cases.

**2.6. Hydrogen Bond Dynamics.** Hydrogen bond dynamics may be studied in molecular dynamics simulations via two different time correlation functions:

$$S_{HB}(t) = \frac{\langle h(0) \cdot H(t) \rangle}{\langle h \rangle} \quad (9)$$

$$C_{HB}(t) = \frac{\langle h(0) \cdot h(t) \rangle}{\langle h \rangle} \quad (10)$$

where the function  $h(t)$  is 1 if a tagged hydrogen bond exists at a time  $t$  and is 0 if it does not, and the function  $H(t)$  is 1 if a tagged hydrogen bond has existed from  $t = 0$  continuously through a time  $t$  and is 0 otherwise. The  $\langle \dots \rangle$  denote averaging over all hydrogen-bonding atom pairs in the molecular dynamics trajectory. The function  $S_{HB}(t)$  is the probability that a hydrogen bond, which is intact at  $t = 0$ , has remained bonded continuously until time  $t$ . The associated relaxation time for this decaying probability density is generally referred to as the average lifetime of a hydrogen bond. The function  $C_{HB}(t)$  is insensitive to interim disruption in the tagged hydrogen bond, and its associated relaxation time may therefore be identified with the structural relaxation of the hydrogen bond network.

The function  $C_{HB}(t)$  is highly nonexponential (see Figure S2(a) in the Supporting Information for a typical example), and to calculate the associated relaxation time would require significant computational resources for a large number of simulations. We therefore calculate relative relaxation times from the equations<sup>40</sup>

$$C_{HB}(t_\delta) = \exp\left(-\frac{t_\delta}{\tau_R}\right) \quad (11)$$

$$\tau_R = \frac{-t_\delta}{\ln C_{HB}(t_\delta)}$$

where  $t_\delta$  is set to 10 ps (the longest time for which we calculate  $C_{HB}(t)$ ). Due to the nonexponential nature of the correlation functions, this value for  $\tau_R$  is an underestimate of the true value, yet the relative time scales of structural relaxation may be compared across simulations and regions. Furthermore, we note that the above calculation does not assume that the function is exponential over any time range (which these functions are not). The estimated “time constant” is simply a measure of the degree of remaining correlation in the hydrogen bond network at time  $t = t_\delta$  (10 ps in this case), converted to a time constant. This measure of correlation suffices for the arguments made below and has been used in the past by other researchers.<sup>40</sup>

The function  $S_{HB}(t)$  decays much faster, as seen in Figure S2(b), and therefore may be integrated numerically so that the lifetime of the hydrogen bond is defined as

$$\tau_{HB} = \int_0^{+\infty} S_{HB}(t) dt \quad (12)$$

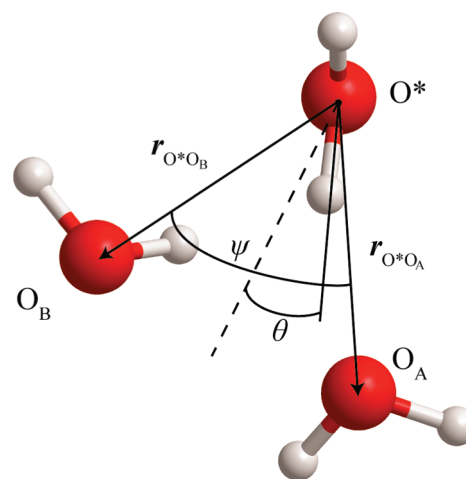


**Figure 2.** Schematic of the hydrogen-bonding exchange coordinate for the rotational jump mechanism. The angle between  $O^*$ ,  $O_B$ , and  $O_A$  is denoted by  $\psi$ . The angle between the angular bisector of  $\psi$  (dashed line) and the  $O^*H$  bond vector is denoted by  $\theta$ .

As Paul and Chandra have observed, the quantity  $\tau_{HB}$  is actually better defined as the average persistence time of a randomly chosen hydrogen bond, since when the hydrogen bond was formed is not included in the calculation of the function.<sup>25</sup> For conciseness and consistency with the literature, we refer to it in this paper as the lifetime of the hydrogen bond.

The correlation functions and associated relaxation times are calculated for all HB pairs in the system and also regional HB pairs. Regional HB pairs are defined as pairs where the donating hydrogen inhabits a region at time zero in the correlation function. Regions are defined as above from the radial density profile of the simulation.

**2.7. Hydrogen Bond Exchange Mechanism and Rate.** To investigate the hydrogen bond exchange mechanism and rate as a function of regional confinement and interface type, we select trajectories of triplets of hydrogen-bonding waters in which a donor hydrogen switches the oxygen to which it is hydrogen bonded. The hydrogen bonds are determined by standard geometrical criteria.<sup>57</sup> A hydrogen bond is counted if the interoxygen distance is less than 3.5 Å, the hydrogen acceptor distance is less than 2.6 Å, and the  $H_d-O_d-O_a$  angle is less than 30°. If the acceptor group is a head group in the AOT RM simulations, then the definition is extended to an interoxygen distance of 5.0 Å and a hydrogen acceptor distance of 4.0 Å.<sup>9,17</sup> Once identified, these trajectories are analyzed with respect to interatomic distances and angles.

A diagram of the coordinates for the exchange process is presented in Figure 2. The quantities averaged are the following: the distances between the oxygen of the hydrogen bond donor ( $O^*$ ) and the first and second oxygens to which the hydrogen bond is formed ( $O_A$  and  $O_B$ ) denoted as  $r_{O^*O_A}$  and  $r_{O^*O_B}$ ; the angle between the  $O^*H^*$  bond vector and the angular bisector of the angle between  $r_{O^*O_A}$  and  $r_{O^*O_B}$  denoted  $\theta$ ; the  $O_A-O^*-O_B$  angle  $\psi$ ; and the number of hydrogen bonds received by  $O^*$ ,  $O_A$ ,  $O_B$ , and donated by  $H^*$  and  $H'$  (the hydrogen not involved in the exchange), denoted as  $n_r^{O^*}$ ,  $n_r^A$ ,  $n_r^B$ ,  $n_d^{H^*}$ , and  $n_d^{H'}$ , respectively. Time zero for the trajectory is defined as the time when  $\theta = 0$ . Since the simulation output occurs on a 4 fs time grid,  $\theta = 0$  is not always satisfied at a particular time step. Therefore, we perform a cubic spline of the  $\theta$  observable, and use Newton's method to find the zero of the now continuous function. A new time grid is

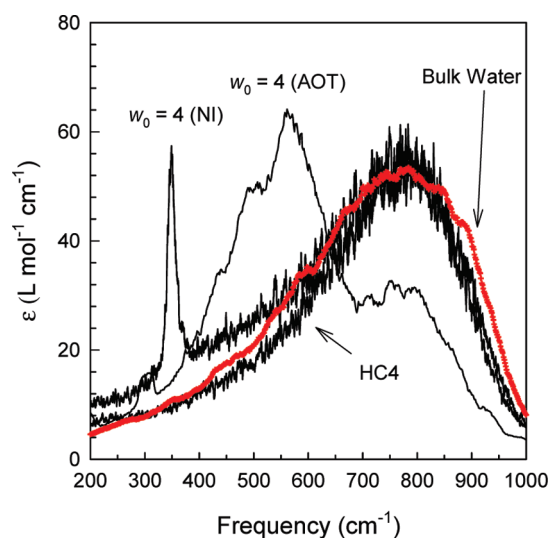


**Figure 3.** Calculated IR spectra for bulk water, NI nanopores, AOT RMs, and HCs. The confined systems are all of size  $w_0 = 4$ . The figure demonstrates that for the NI interfaces the perturbation to the librational frequency of liquid water is negligible. The sharp peak and the associated tails in the NI nanopore at around  $350\text{ cm}^{-1}$  are due to the translation of the head groups. This was verified through selective Fourier–Laplace transformations of decompositions of the total system dipole autocorrelation function and variation of the head-group harmonic potential.

constructed and all other observables are interpolated onto this new grid.

The forward rate constant for hydrogen bond exchanges may be calculated from the decay of the time correlation function

$$1 - \langle n_A(0) \cdot n_B(t) \rangle \quad (13)$$

where the function  $n_X(t)$  is 1 if a hydrogen bond exists between a chosen hydrogen and the oxygen X. Virtually absorbing conditions are used for the exchange so that once the hydrogen bond switches from A to B the function remains zero. This ensures that the calculation does not average in reverse exchange and will decay with the forward rate constant only. Regional hydrogen bonds are defined by the location of the donating molecule at time zero. We report the average time before exchange for a hydrogen bond defined by the time constant for the decay of the correlation function given in eq 13. The rate constant for hydrogen bond exchange is simply

$$k_{\text{exch}} = \frac{1}{\tau_{\text{exch}}} \quad (14)$$

### 3. RESULTS AND DISCUSSION

**3.1. Calculated Infrared Spectra of Confined Aqueous Systems.** Figure 3 presents the calculated infrared spectra of ionic RMs, NI nanopores, HCs, and bulk water between 200 and  $1000\text{ cm}^{-1}$ . The calculated infrared spectrum in the AOT RM simulation shows a red-shifted peak associated with the bound and trapped water. The NI nanopores and HCs do not show this peak and have bulklike librational IR spectra. For the NI case there is a sharp low-frequency peak with a tail which extends into the water librational region, but this peak is associated with translational motion of the head groups and may be numerically removed by separating the dipole–dipole autocorrelation function into its water and head group components.

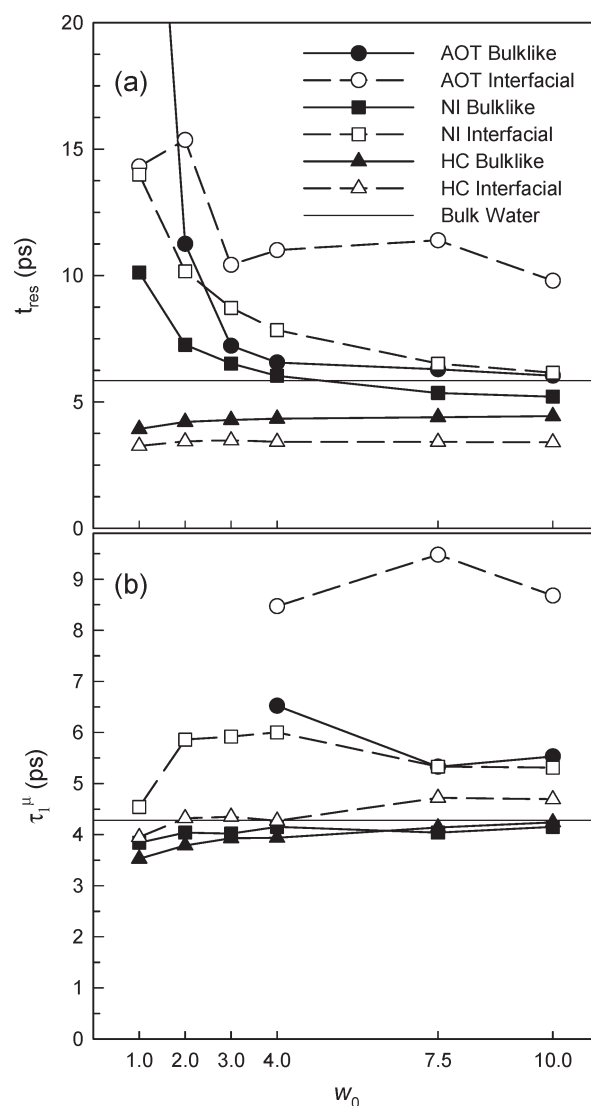


**Figure 4.** (a) Residence times for all regions and types of nanopores. See text for discussion. (b) Orientational correlation times for water confined within all regions of each type of nanopore.  $w_0 = 1$  through  $w_0 = 3$  are not shown for ionic head groups due to potentially anomalous results for those nanopores.

The nature of the infrared absorbance for AOT RMs has been previously explained as a decrease in water–water hydrogen bonding and a decrease in hydrogen bond strength in the trapped water layer.<sup>17,18</sup> The bulklike spectra for NI nanopores and HCs demonstrate that the local potential energy surface even in these highly nonbulk environments is on average nearly the same as the bulk. It also demonstrates that the transient motion of the water molecules in these nanoscopic pools is on average the same as that in the bulk.

**3.2. Translational Mobility.** Translational residence times for water in bulk and the various types of confined water under investigation in this study are reported in Figure 4a (and Tables S2–S4 in the Supporting Information). In NI nanopores, water at the interface diffuses more slowly than the bulk, and the interior water pool gradually recovers the bulk diffusive behavior. In HCs the water diffuses much faster at the interface than in the bulk, and water in the interior also gradually recovers the bulk diffusive behavior. In ionic AOT RMs, there is some size dependence to the

translational mobility in the various regions. For the larger AOT RMs the bound water layer diffuses slower than that of the bulklike interior, whereas for the smallest RMs the bulklike interior diffuses slower than the bound layer. This phenomenon has been previously shown by Faeder and Ladanyi,<sup>9</sup> and we attribute it to the small number of water molecules which inhabit the bulklike region in the smallest AOT RMs; for example, there is essentially no bulklike water in  $w_0 = 1$ . We also note that the very large total system residence time in the AOT RMs may be attributed to the trapped water layer which diffuses on a much slower time scale than either the bound or the bulklike layer.

The average relative change in the translational mobility between interior water pool and interfacial layer for the various systems reflects the differences in the degrees of perturbation. We define the average relative change as the ratio of the interfacial translational residence time to the bulklike interior translational residence time. For AOT RMs the average relative change to the translational residence time is 1.58, and for NI nanopores it is 1.30. This demonstrates that the highly ionic interface of AOT RMs perturbs the bound water layer more strongly than the oriented dipoles of the NI nanopores. The fact that the average relative change to the translational residence time for the HC is 0.80 is consistent with the fact that the interfacial water does not interact with the nanopore surface.

The trends illustrated in this translational mobility data have important ramifications for the time evolution of the hydrogen bond network which has long-time components dominated by diffusion.

**3.3. Orientational Dynamics.** Figure 4b (and Tables S5–S7 in the Supporting Information) shows that all three interfaces slow down the orientational dynamics of water. Several important trends are clear. The HC simulations show almost no difference at the interface relative to bulk water, but slightly faster dynamics relative to bulk in the interior. The dynamics at the interface of NI nanopores are always slower than bulk, and always slower than the interior of the water pool whose dynamics are almost identical to that found in bulk water; this difference between interfacial and interior dynamics is larger relative to that found in the HCs. Both NI nanopores and HCs differ from the ionic RMs where the slowdown in dynamics penetrates to the interior of the RM, and the slowdown in the interfacial region is much larger in magnitude, roughly a factor of 2.

The rotational dynamics of water are inherently connected to the hydrogen bond dynamics of water, since for the rotational correlation to decay to zero the water–water hydrogen bond network must also lose all correlation with its former state. These reorientation times therefore are rough estimates for the hydrogen bond exchange times which will be rigorously calculated below. A comparison between the hydrogen bond exchange times and the dynamics suggested by the reorientation times will be performed in section 3.5.

**3.4. Hydrogen Bond Dynamics.** The functions  $C_{HB}(t)$  and  $S_{HB}(t)$  were calculated for bulk water and ionic, NI, and hydrophobic RMs of sizes  $w_0 = 1$  through  $w_0 = 10$ . These functions were also calculated for water molecules in different regions (spherical shells) of the simulations. For the ionic RMs, the correlation functions were calculated for trapped, bound, and bulklike water. For NI nanopores and HCs, the functions were calculated for interfacial and bulklike water. The regions were defined by the minima in the radial density of oxygen in the simulations as discussed above. The associated relaxation times were extracted via the methods outlined above and are reported in Figure 5a

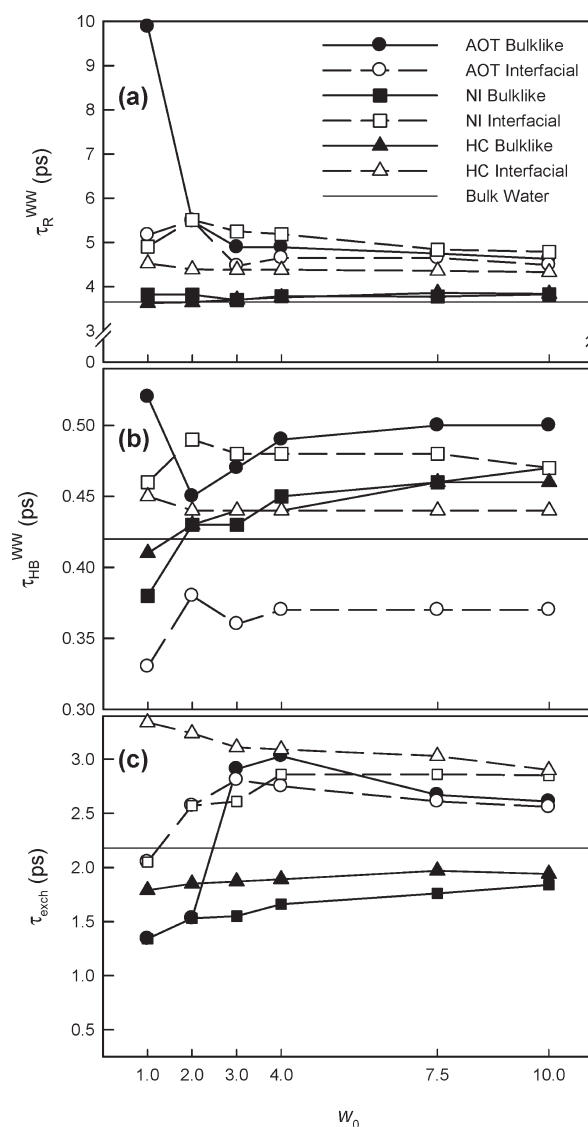


**Figure 5.** (a) Hydrogen bond network ( $C_{HB}(t)$ ) relaxation times for all regions and nanopore types. (b) Hydrogen bond lifetimes ( $S_{HB}(t)$ ) for all regions and nanopore types. (c) Hydrogen bond exchange for all regions and nanopores. See text for discussion.

(and Tables S8–S10 in the Supporting Information). The hydrogen bond lifetimes (from  $S_{HB}(t)$ ) are reported in Figure 5b (and Tables S8–S10 in the Supporting Information).

For the NI case several important trends are clear. The hydrogen bond network near the interface always relaxes slower than the network in the inner water pool (Figure 5a), and the hydrogen bonds at the interface survive longer than the hydrogen bonds in the interior (Figure 5b). The slow structural relaxation at the interface is akin to the slow structural relaxation of water in an ionic atmosphere (aqueous ionic solutions) where slower diffusion causes slower relaxation. The slower diffusion at the interface relative to the interior of the NI RM partially accounts for the slower structural relaxation. Since water cannot diffuse away from its prior hydrogen-bonding partner, it is more likely to re-form the same hydrogen bond and thus lengthen the time that the hydrogen bond network remains self-correlated. The slowdown in hydrogen bond network dynamics also occurs in the bulklike interior, although this effect is not pronounced.



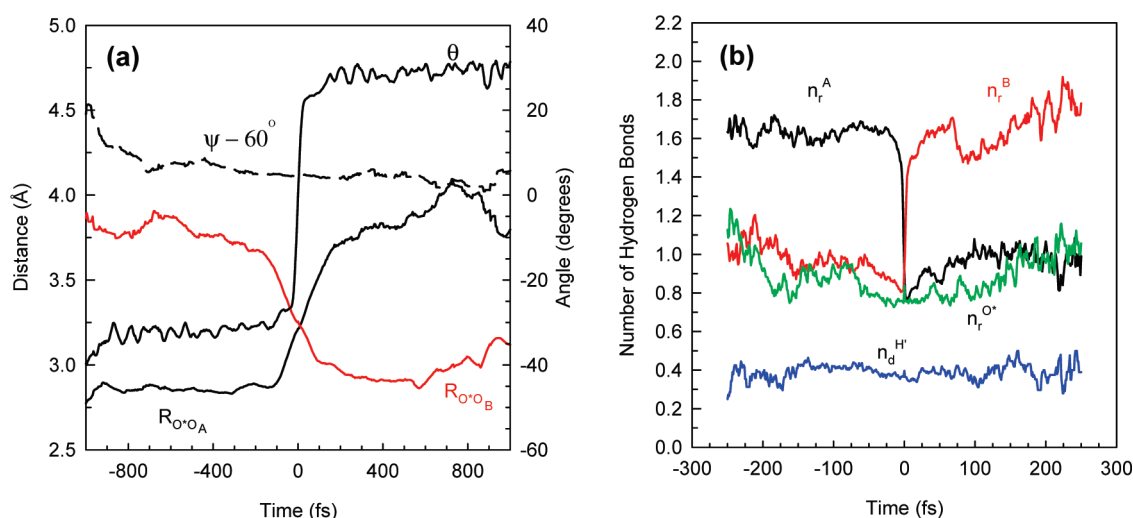


**Figure 6.** Hydrogen bond exchange mechanism reaction coordinate plots for interfacial water in AOT RMs. As in the text, water molecule A is initially accepting a hydrogen bond which rapidly switches to water molecule B. (a)  $R_{O^*O_A}$  is the distance between  $O^*$ , the oxygen of the hydrogen-bond-donating water, and the oxygen on hydrogen bond acceptor A.  $R_{O^*O_B}$  is the corresponding distance for the oxygen on water molecule B.  $\psi - 60^\circ$  is the angle between  $O^*$ ,  $O_A$ , and  $O_B$  minus  $60^\circ$  (for ease of plotting).  $\theta$  is the angle between the  $O^*-H$  bond vector and the angular bisector of  $\psi$ . (b)  $n_r^A$  is the number of hydrogen bonds received by oxygen A, and  $n_r^B$  is the corresponding value for oxygen B.  $n_r^{O^*}$  is the number of hydrogen bonds donated by the other hydrogen on the hydrogen-bond-donating molecule (which contains  $O^*$ ).  $n_d^{H'}$  is the number of hydrogen bonds received by the oxygen on the water molecule donating the hydrogen bond that is undergoing exchange. See text for a full discussion.

The longer average hydrogen bond lifetimes at the interface relative to the interior are readily explained by the mechanism of hydrogen bond exchange. In order to undergo hydrogen bond exchange, a water molecule must have a readily available hydrogen-bonding partner in the second hydration shell.<sup>43,44</sup> At the interface, the number of nearest-neighbor water molecules decreases. This decreases the probability of there being a nearby water molecule that may accept a newly formed hydrogen bond and thus lengthens the lifetime of already formed hydrogen bonds. Thus, the function  $S_{HB}(t)$  decays slower at the interface than in the bulklike interior. The effect of the interface on the function  $S_{HB}(t)$  is limited in magnitude since the function is dominated by the breaking of the hydrogen bond by libration. Another method of looking at hydrogen bond dynamics through the rate of exchange will be examined in the following section.

Within ionic RMs, the interfacial water hydrogen bond network relaxes at nearly the same rate as the bulklike interior, although this interior decay rate is significantly slower than the bulk (Figure 5a). We attribute the slowdown in the interior to the long-range effects of this type of interface, particularly on slower diffusive transport. However, several other factors affect the decay of the function  $C_{HB}(t)$ , namely, the nearest-neighbor density and hydrogen bond strength. In the bound region of ionic RMs there is a relative increase in the density of water. This increases the local nearest-neighbor density giving water more hydrogen-bonding partners to exchange to and subsequently cause decorrelation in the hydrogen bond network. Also, the hydrogen bond strength in this region decreases from the bulklike interior due to the perturbing ionic interface. This is evident in the much decreased average hydrogen bond lifetimes for the bound region relative to the interior (Figure 5b), and the decreased librational frequency. Exchange will occur faster since the entire region has weaker hydrogen bonds. Both of these effects counter the slowdown in diffusion and are likely culprits for the faster than expected structural relaxation in the interfacial layer.

The HC simulations show faster hydrogen bond network dynamics in the interior of the cavity, almost the same as bulk, as seen in Figure 5a. This is most easily explained by the much higher translational mobility of water in the hydrophobic cavity even far from the interface. The interfacial water, even though it has a higher mobility than that in the interior, undergoes slower structural relaxation. Other workers have shown the origin to be stronger hydrogen bonds at the interface.<sup>25</sup> The slowdown in the structural relaxation of the interfacial water is also correlated with a decrease in the hydrogen bond exchange rate, which is most likely due to the decreased nearest-neighbor density at the interface. The average hydrogen bond lifetime does not change much at the interface relative to the interior (Figure 5b). This is due to the strong dependence of this quantity on librational breaking of hydrogen bonds.

**3.5. Hydrogen Bond Exchange Mechanism and Rate.** Figure 6 shows the average hydrogen bond exchange mechanism for interfacial water in AOT RMs in terms of the reaction coordinates defined in section 2.7. The interfacial water in the AOT RM system exchanges hydrogen bonds via the rotational jump mechanism.<sup>58</sup> This mechanism is characterized by an ultrafast jump in the  $\theta$  coordinate along with a simultaneous increase in  $R_{O^*O_A}$  and decrease in  $R_{O^*O_B}$ . We find this mechanism to be independent of the environment of the water—bulklike or interfacial, ionic RMs, NI nanopores, and HCs alike. The mechanistic data were calculated for the  $w_0 = 4$  size AOT RMs, NI nanopores, and HCs by the methods described above. The behavior of water in the NI nanopores and HCs, as well as the bulklike water in the ionic RMs, is nearly identical to bulk water<sup>58</sup> (as seen in Figures S3–S7 in the Supporting Information). Furthermore, the difference between interfacial water in the AOT RMs (Figure 6) and bulk water lies in the number of hydrogen bonds accepted by  $O^*$  and donated by  $H'$  (the hydrogen not involved with the exchange), and not the time scale or mechanism of the hydrogen bond jump.

As in bulk water, the number of hydrogen bonds received by  $O_A$  decreases at the instant of the jump, with a concomitant



increase in the number of hydrogen bonds received by  $O_B$ . However, the magnitude of the change in number of hydrogen bonds is roughly 60% larger than in bulk water.<sup>58</sup> In bulk water, the average number of hydrogen bonds accepted by  $O_B$  changes from about 1.5 to 2.1 at the instant of the jump,<sup>58</sup> whereas we find the average number changes from about 0.9 to 1.6 for the interfacial water in the ionic RM. This is due to the fact that the presence of  $Na^+$  ions in the trapped region will reduce the number of hydrogen bonds that water in the interfacial region will accept. The number of hydrogen bonds received by  $O^*$  and the number donated by  $H'$  are both roughly 50% smaller than bulk,<sup>58</sup> and again, this is a result of the decreased water–water hydrogen bonding at the AOT interface.<sup>17</sup>

The reaction proceeds through a transition state where the hydrogen bond is bifurcated and is driven by coordinated fluctuations in hydrogen bond number of the three molecules involved in exchange. The rotational jump occurs on a subpicosecond time scale. In order to quantify the time scale of the rotational jump, we calculated the first time derivative of the averaged  $\theta$  coordinate. We find that the full width at half-maximum (fwhm) is roughly 40 fs. This time is the time scale of the steepest part of the sigmoid-like function  $\theta$ . Although this time is shorter than the approximate number that Laage and Hynes report for bulk water ( $\sim 250$  fs), their visual approximation includes the relatively long “tails” in the  $\theta$  coordinate.<sup>44,58</sup> All of the systems perform the rotational jump on the order of 40 fs which indicates that the actual exchange of the hydrogen bond along successful trajectories is independent of the microenvironment of the water involved.

We have calculated the rates of hydrogen bond exchange for the same four systems as above using the time correlation method described at the end of section 2.6. In Figure 5c (and Tables S11–S13 in the Supporting Information) we report the average time before hydrogen bond exchange for a randomly chosen hydrogen bond. Longer times indicate slower hydrogen bond network evolution and shorter times represent faster hydrogen bond network dynamics. For NI nanopores and HCs, the interfacial exchange times are much longer than that for interior water, demonstrating slow hydrogen bond dynamics at the interface. This is consistent with recent work investigating hydrogen bond exchange around hydrophobic solutes, where it was found that the excluded volume by the hydrophobic solute slowed down exchange.<sup>59</sup> Also, previous work has suggested that the availability of a new hydrogen bond acceptor is in some sense a rate-limiting step for the exchange of a hydrogen bond.<sup>43</sup> In the NI and HC simulations, the lower nearest-neighbor density at the interface produces a similar effect in the hydrogen bond exchange rates. The interior exchange times are faster than bulk water at small sizes but increase gradually toward the bulk limit.

The behavior in the ionic RMs is more complicated. At small sizes, the exchange times in the bound region are longer than that for water in the “interior”. However, due to the fact that bulklike water is ill-defined when  $w_0 < 3$ , we believe the results at small sizes to be anomalous. In the larger RMs, where the water species are well-defined, the exchange times in bulklike and bound water are identical within the presumed error of the simulations. This is in stark contrast to the orientational dynamics illustrated by the single dipole autocorrelation functions, where the interfacial water reorients more slowly. In bulk water the orientational relaxation of the liquid is governed by the hydrogen bond network relaxation—one type of relaxation cannot occur without the other. Yet, inside an ionic RM it is well-known that there is

a strong dipolar polarization along the radial direction.<sup>9</sup> The bound water has a net polarization with respect to the surface normal whereas the bulklike water does not. This average preference for the water dipoles to align toward the interface suggests a net preference for hydrogen bond exchanges which preserve a radial dipole polarization. Such a preference induced by interactions with the interface would produce longer time correlations in the orientational correlation functions which would not necessarily be coupled to hydrogen bond exchange. Furthermore, since the number of hydrogen bonds is decreased near the interface due to the solvation of sodium counterions,<sup>13,17</sup> the components of orientational relaxation not related to hydrogen bond exchange become more important. Since the slowing of reorientational dynamics is independent of the hydrogen bond exchange dynamics, it is suggested that these mechanisms of reorientation are slower than the reorientation mechanisms in bulklike water. Further investigation of the differences between hydrogen bond network evolution and rotational dynamics at complex interfaces is an important future direction of investigation, but is beyond the scope of this paper.

#### 4. CONCLUSION

The effects of confinement in spherical nanopores with three different types of interface have been analyzed by molecular dynamics simulations. We have focused on the interfacial and bulklike water regions within these small cavities. We have ignored water that is trapped within the ionic head groups of these nanostructures due to its incredibly long relaxation time scale, and also the sequestering of this water from the interior water network.

Several trends have been uncovered. Within NI nanopores and HCs, the hydrogen bond network relaxes more slowly at the interface, and the hydrogen bond exchange also slows at the interface. In the interior these processes occur slightly faster than the bulk but approach the bulk value as nanopore size increases. The overall network correlation decays more slowly at both interfaces compared to the interior despite the differences in diffusive transport. This is due to the well-known result that there is a relative increase in hydrogen bonding at a hydrophobic interface.<sup>9,28,36</sup> Rotational motion is slowed at the interface, which is expected due to the slower hydrogen bond dynamics. The librational frequencies of the water at these interfaces are unchanged and therefore the nonintermittent hydrogen bond time correlation function ( $S_{HB}$ ) decays at the same rate in NI nanopores and HCs.

AOT ionic RMs have several countervailing trends relative to the NI nanopores and HCs. Despite having slower rotational dynamics in the interfacial layer than in the bulklike interior, interfacial water and bulklike water show essentially the same hydrogen bond dynamics. This is surprising due to the interdependencies of these two phenomena, namely that the rotational decorrelation can only occur when randomization of the hydrogen bond network has occurred. We have suggested reasons behind this phenomena through the substantial polarization present in the interfacial layer and the changes in density and diffusion within this layer. Also, because there are fewer hydrogen bonds for the bound water molecules in AOT RMs, it is plausible that the non-hydrogen bond network based mechanisms of reorientation are slow in this region.

Experimentally, NI and ionic RMs both show strong perturbations to water structure and dynamics.<sup>15,30</sup> Yet, in these simulations we have shown that a simple NI nanopore with a hydroxylated interface produces no change in the librational frequencies and

therefore the populations of different hydrogen-bonding environments. This suggests that it is the water trapped within the head groups of a NI RM that contributes most strongly to the weakened hydrogen bonding states that have been observed by IR spectroscopy of the OH stretch.<sup>30</sup> Unfortunately, experimental studies of the librational band in NI RMs do not exist, so it is not known whether or not the simulation results agree with experimental results in that region of the spectrum. On a more general note, we find that simple confinement in a nanopore, such as HCs, produces only modest perturbations to water structure and dynamics relative to systems which have strong interfacial trapping characteristics, such as ionic RMs.

The rotational jump mechanism has been shown to be robust in several heterogeneous environments. The mechanism does not depend on the nearest neighbor density, system geometry or perturbations to the bulk water potential energy surface, or even the average number of hydrogen bonds donated and accepted. This is consistent with the more recent work of Laage and Hynes which has found changes in the hydrogen bond exchange time (but not the hydrogen bond exchange mechanism) in the presence of solutes due to the excluded volume effect.<sup>59</sup>

## ■ ASSOCIATED CONTENT

**S Supporting Information.** Table S1 specifies the atomistic model parameters used for the simulations. Tables S2–S13 present the raw data used to generate Figures 4 and 5 in the text. Figures S1 and S2 show time correlation functions [orientational;  $CHB(t)$ ; and  $SHB(t)$ ]. Figure S3 shows the molecular jump mechanism and average number of hydrogen bonds for bulk water. Figures S4–S8 show the same information for bulklike water in ionic RMs, bulklike, and interfacial water in NI RMs, and bulklike and interfacial water in HCs. This material is available free of charge via the Internet at <http://pubs.acs.org>.

## ■ AUTHOR INFORMATION

### Corresponding Author

\*E-mail: [daniel.rosenfeld@stanford.edu](mailto:daniel.rosenfeld@stanford.edu) (D.E.R.), [charles.schmuttermaer@yale.edu](mailto:charles.schmuttermaer@yale.edu) (C.A.S.).

### Present Addresses

<sup>†</sup>Department of Chemistry, Stanford University, Stanford, CA 94305.

## ■ ACKNOWLEDGMENT

D.E.R. thanks the Arnold and Mabel Beckman Foundation for support under the Beckman Scholars Program.

## ■ REFERENCES

- (1) Tan, H. S.; Piletic, I. R.; Riter, R. E.; Levinger, N. E.; Fayer, M. D. *Phys. Rev. Lett.* **2005**, *94*, 057405.
- (2) Tan, H. S.; Piletic, I. R.; Fayer, M. D. *J. Chem. Phys.* **2005**, *122*, 174501.
- (3) Piletic, I. R.; Tan, H. S.; Fayer, M. D. *J. Phys. Chem. B* **2005**, *109*, 21273.
- (4) Piletic, I. R.; Moilanen, D. E.; Spry, D. B.; Levinger, N. E.; Fayer, M. D. *J. Phys. Chem. A* **2006**, *110*, 4985.
- (5) Amararene, A.; Gindre, M.; LeHuerou, J. Y.; Nicot, C.; Urbach, W.; Waks, M. *J. Phys. Chem. B* **1997**, *101*, 10751.
- (6) Boyd, J. E.; Briskman, A.; Sayes, C. M.; Mittleman, D.; Colvin, V. *J. Phys. Chem. B* **2002**, *106*, 6346.
- (7) Brown, D.; Clarke, J. H. R. *J. Phys. Chem.* **1988**, *92*, 2881.
- (8) D'Angelo, M.; Onori, G.; Santucci, A. *J. Phys. Chem.* **1994**, *98*, 3189.
- (9) Faeder, J.; Ladanyi, B. M. *J. Phys. Chem. B* **2000**, *104*, 1033.
- (10) Faeder, J.; Ladanyi, B. M. *J. Phys. Chem. B* **2001**, *105*, 11148.
- (11) Faeder, J.; Albert, M. V.; Ladanyi, B. M. *Langmuir* **2003**, *19*, 2514.
- (12) Faeder, J.; Ladanyi, B. M. *J. Phys. Chem. B* **2005**, *109*, 6732.
- (13) Harpham, M. R.; Ladanyi, B. M.; Levinger, N. E.; Herwig, K. W. *J. Chem. Phys.* **2004**, *121*, 7855.
- (14) Harpham, M. R.; Ladanyi, B. M.; Levinger, N. E. *J. Phys. Chem. B* **2005**, *109*, 16891.
- (15) Onori, G.; Santucci, A. *J. Phys. Chem.* **1993**, *97*, 5430.
- (16) Sando, G. M.; Dahl, K.; Owrtusky, J. C. *J. Phys. Chem. A* **2004**, *108*, 11209.
- (17) Rosenfeld, D. E.; Schmuttermaer, C. A. *J. Phys. Chem. B* **2006**, *110*, 14304.
- (18) Venables, D. S.; Huang, K.; Schmuttermaer, C. A. *J. Phys. Chem. B* **2001**, *105*, 9132.
- (19) Pieniazek, P. A.; Lin, Y. S.; Chowdhary, J.; Ladanyi, B. M.; Skinner, J. L. *J. Phys. Chem. B* **2009**, *113*, 15017.
- (20) Chowdhary, J.; Ladanyi, B. M. *J. Phys. Chem. B* **2009**, *113*, 15029.
- (21) Castrillon, S. R. V.; Giovambattista, N.; Aksay, I. A.; Debenedetti, P. G. *J. Phys. Chem. B* **2009**, *113*, 1438.
- (22) Vasilescu, M.; Caragheorgheopol, A.; Almgren, M.; Brown, W.; Alsins, J.; Johannsson, R. *Langmuir* **1995**, *11*, 2893.
- (23) Scodinu, A.; Fourkas, J. T. *J. Phys. Chem. B* **2002**, *106*, 10292.
- (24) Rovere, M.; Ricci, M. A.; Vellati, D.; Bruni, F. *J. Chem. Phys.* **1998**, *108*, 9859.
- (25) Paul, S.; Chandra, A. *Chem. Phys. Lett.* **2004**, *386*, 218.
- (26) Pant, D.; Levinger, N. E. *Langmuir* **2000**, *16*, 10123.
- (27) Lopez, C. F.; Nielsen, S. O.; Klein, M. L.; Moore, P. B. *J. Phys. Chem. B* **2004**, *108*, 6603.
- (28) Lee, S. H.; Rossky, P. J. *J. Chem. Phys.* **1994**, *100*, 3334.
- (29) Dokter, A. M.; Woutersen, S.; Bakker, H. J. *J. Chem. Phys.* **2007**, *126*, 124507.
- (30) Brubach, J. B.; Mermet, A.; Filabozzi, A.; Gerschel, A.; Lairez, D.; Krafft, M. P.; Roy, P. *J. Phys. Chem. B* **2001**, *105*, 430.
- (31) Abel, S.; Waks, M.; Marchi, M.; Urbach, W. *Langmuir* **2006**, *22*, 9112.
- (32) Chanda, J.; Bandyopadhyay, S. *J. Chem. Theory Comput* **2005**, *1*, 963.
- (33) Sterpone, F.; Pierleoni, C.; Briganti, G.; Marchi, M. *J. Phys. Chem. B* **2006**, *110*, 18254.
- (34) Sterpone, F.; Marchetti, G.; Pierleoni, C.; Marchi, M. *J. Phys. Chem. B* **2006**, *110*, 11504.
- (35) Xu, H. F.; Berne, B. J. *J. Phys. Chem. B* **2001**, *105*, 11929.
- (36) Lee, C. Y.; Mccammon, J. A.; Rossky, P. J. *J. Chem. Phys.* **1984**, *80*, 4448.
- (37) Chowdhary, J.; Ladanyi, B. M. *J. Phys. Chem. B* **2009**, *113*, 4045.
- (38) Luzar, A.; Chandler, D. *Nature* **1996**, *379*, 55.
- (39) Luzar, A.; Chandler, D. *Phys. Rev. Lett.* **1996**, *76*, 928.
- (40) Chandra, A. *Phys. Rev. Lett.* **2000**, *85*, 768.
- (41) Chanda, J.; Bandyopadhyay, S. *J. Phys. Chem. B* **2006**, *110*, 23443.
- (42) Balasubramanian, S.; Pal, S.; Bagchi, B. *Phys. Rev. Lett.* **2002**, *89*, 115505.
- (43) Laage, D.; Hynes, J. T. *Chem. Phys. Lett.* **2006**, *433*, 80.
- (44) Laage, D.; Hynes, J. T. *Science* **2006**, *311*, 832.
- (45) Eicke, H. F.; Rehak, J. *Helv. Chim. Acta* **1976**, *59*, 2883.
- (46) Jorgensen, W. L.; Madura, J. D.; Swenson, C. J. *J. Am. Chem. Soc.* **1984**, *106*, 6638.
- (47) Wilson, M. A.; Pohorille, A. *J. Am. Chem. Soc.* **1994**, *116*, 1490.
- (48) Fincham, D. *Mol. Simul.* **1992**, *8*, 165.
- (49) Berendsen, H. J. C.; Grigera, J. R.; Straatsma, T. P. *J. Phys. Chem.* **1987**, *91*, 6269.
- (50) Tildesley, D. J.; Allen, M. P. *Computer Simulation of Liquids*; Clarendon Press: Oxford, UK, 1987.
- (51) Berendsen, H. J. C.; Postma, J. P. M.; van Gunsteren, W. F.; DiNola, A.; Haak, J. R. *J. Chem. Phys.* **1984**, *81*, 3684.
- (52) Caillol, J. M.; Levesque, D.; Weis, J. J. *J. Chem. Phys.* **1986**, *85*, 6645.

- (53) Ahlborn, H.; Space, B.; Moore, P. B. *J. Chem. Phys.* **2000**, *112*, 8083.
- (54) Ahlborn, H.; Ji, X. D.; Space, B.; Moore, P. B. *J. Chem. Phys.* **1999**, *111*, 10622.
- (55) Liu, P.; Harder, E.; Berne, B. J. *J. Phys. Chem. B* **2004**, *108*, 6595.
- (56) Bizzarri, A. R.; Rocchi, C.; Cannistraro, S. *Chem. Phys. Lett.* **1996**, *263*, 559.
- (57) Luzar, A.; Chandler, D. *J. Chem. Phys.* **1993**, *98*, 8160.
- (58) Laage, D.; Hynes, J. T. *J. Phys. Chem. B* **2008**, *112*, 14230.
- (59) Laage, D.; Stirnemann, G.; Hynes, J. T. *J. Phys. Chem. B* **2009**, *113*, 2428.



## Supporting Information

### Dynamics of the Water Hydrogen Bond Network at Ionic, Nonionic and Hydrophobic Interfaces in Nanopores and Reverse Micelles

Daniel E. Rosenfeld<sup>\*,a)</sup> and Charles A. Schmuttenmaer<sup>\*</sup>  
*Yale University, Department of Chemistry, 225 Prospect St., P. O. Box 208107  
 New Haven, CT 06520-8107, USA*

<sup>a)</sup>*Present Address: Department of Chemistry, Stanford University, Stanford, CA 94305, USA*

October 6, 2010

This document contains supplementary tables on pages 1 – 5, and supplementary figures on pages 6 – 9.

#### I. Supplementary Tables

Table S1 specifies the atomistic model parameters used for the simulations. Tables S2 – S13 present the raw data used to generate Figures 4 and 5 in the text. A full discussion of all results is in the main text of the article.

**Table S1.** Interaction potential parameters. The Lennard-Jones radius and well depth are given by  $\sigma$  and  $\varepsilon$ , respectively, and  $q$  is the charge on a particular site. The subscript (HG) denotes parameters used for the NI nanopore simulations.

	$\sigma$ (Å)	$\varepsilon/k_B$ (K)	$q$ (e)
O	3.166	78.24	-0.8476
H	—	—	0.4238
Na <sup>+</sup>	2.275	58.01	1.0
Z <sup>-</sup>	6.0	251.58	-1.0
wall	2.5	231.55	—
O <sub>(HG)</sub>	3.07	85.591	-0.60
H <sub>(HG)</sub>	—	—	0.35
CH <sub>2</sub> <sub>(HG)</sub>	3.905	59.40	0.25

**Table S2.** Translational residence times for NI nanopores. ( $d > d_{int}$ ) denotes water in the interior of the nanopore which is bulklike. ( $d < d_{int}$ ) denotes interfacial water.

	$t_{res}$ (ps)	$t_{res}$ ( $d > d_{int}$ ) (ps)	$t_{res}$ ( $d < d_{int}$ ) (ps)
Bulk	5.85	—	—
$w_0 = 1$ (NI)	13.11	10.12	13.99
$w_0 = 2$ (NI)	9.67	7.26	10.17
$w_0 = 3$ (NI)	8.19	6.52	8.72
$w_0 = 4$ (NI)	7.34	6.03	7.84
$w_0 = 7.5$ (NI)	5.99	5.35	6.51
$w_0 = 10$ (NI)	5.66	5.21	6.15

**Table S3.** Translational residence times for hydrophobic cavities. Regions are as in Table S2.

	$t_{res}$ (ps)	$t_{res}$ ( $d > d_{int}$ ) (ps)	$t_{res}$ ( $d < d_{int}$ ) (ps)
Bulk	5.85	—	—
HC1	3.39	3.93	3.26
HC2	3.65	4.21	3.44
HC3	3.76	4.29	3.48
HC4	3.77	4.34	3.42
HC7.5	3.93	4.40	3.42
HC10	4.01	4.44	3.40

**Table S4.** Translational residence times for ionic RMs. ( $d > d_{int}$ ) denotes water in the interior of the nanopore which is bulklike. ( $1.5 < d < d_{int}$ ) denotes interfacial water. The trapped water is not included due its very slow dynamics and lack of similarity to interfacial water in the other systems.

	$t_{res}$ (ps)	$t_{res}$ ( $d > d_{int}$ ) (ps)	$t_{res}$ ( $1.5 < d < d_{int}$ ) (ps)
Bulk	5.85	—	—
$w_0 = 1$ (AOT)	20.90*	37.01*	14.31
$w_0 = 2$ (AOT)	21.70*	11.25	15.36*
$w_0 = 3$ (AOT)	13.84	7.22	10.42
$w_0 = 4$ (AOT)	12.43	6.56	11.00
$w_0 = 7.5$ (AOT)	9.34	6.29	11.39
$w_0 = 10$ (AOT)	8.01	6.04	9.79

**Table S5.** Orientational relaxation times for NI nanopores. Regions are as in Table S2.

	$\tau_1^{\hat{\mu}}$ (ps)	$\tau_1^{\hat{\mu}}$ ( $d > d_{int}$ ) (ps)	$\tau_1^{\hat{\mu}}$ ( $d < d_{int}$ ) (ps)
Bulk	4.28	—	—
$w_0 = 1$ (NI)	4.47	3.84	4.54
$w_0 = 2$ (NI)	5.62	4.04	5.86
$w_0 = 3$ (NI)	5.57	4.02	5.92
$w_0 = 4$ (NI)	5.63	4.15	6.00
$w_0 = 7.5$ (NI)	4.85	4.04	5.33
$w_0 = 10$ (NI)	4.79	4.15	5.31

**Table S6.** Orientational relaxation times for HCs. Regions are as in Table S2.

	$\tau_1^{\hat{\mu}}$ (ps)	$\tau_1^{\hat{\mu}} (d > d_{int})$ (ps)	$\tau_1^{\hat{\mu}} (d < d_{int})$ (ps)
Bulk	4.28	—	—
HC1	3.84	3.53	3.95
HC2	4.15	3.79	4.32
HC3	4.18	3.93	4.35
HC4	4.13	3.94	4.27
HC7.5	4.38	4.14	4.72
HC10	4.39	4.24	4.69

**Table S7.** Orientational relaxation times for ionic RMs. Regions are as in Table S4.

	$\tau_1^{\hat{\mu}}$ (ps)	$\tau_1^{\hat{\mu}} (d > d_{int})$ (ps)	$\tau_1^{\hat{\mu}} (1.5 < d < d_{int})$ (ps)
Bulk	4.28	—	—
$w_0 = 4$ (AOT)	—	6.52	8.47
$w_0 = 7.5$ (AOT)	—	5.33	9.48
$w_0 = 10$ (AOT)	—	5.53	8.68

**Table S8:** Hydrogen bond network time constants from MD simulations of model NI RMs for water–water hydrogen bonds. The columns labeled  $(d < d_{int})$  denote interfacial water as and the columns labeled  $(d > d_{int})$  denote bulklike water in the center of the RM. The superscript  $WW$  denotes water–water hydrogen bonds and the superscript ‘all’ includes the entire hydrogen bond network including water–headgroup hydrogen bonds.

	$\tau_R^{WW}$ (ps)	$\tau_R^{WW}$ ( $d > d_{int}$ ) (ps)	$\tau_R^{all}$ ( $d < d_{int}$ ) (ps)	$\tau_R^{WW}$ ( $d < d_{int}$ ) (ps)	$\tau_{HB}^{WW}$ (ps)	$\tau_{HB}^{WW}$ ( $d > d_{int}$ ) (ps)	$\tau_{HB}^{WW}$ ( $d < d_{int}$ ) (ps)
Bulk	3.66	—	—	—	0.42	—	—
$w_0 = 1$ (NI)	4.56	3.82	4.91	4.68	0.44	0.38	0.46
$w_0 = 2$ (NI)	4.92	3.82	5.51	5.13	0.48	0.43	0.49
$w_0 = 3$ (NI)	4.78	3.70	5.25	5.06	0.47	0.43	0.48
$w_0 = 4$ (NI)	4.88	3.79	5.19	5.19	0.47	0.45	0.48
$w_0 = 7.5$ (NI)	4.49	3.78	4.84	4.93	0.47	0.46	0.48
$w_0 = 10$ (NI)	4.40	3.83	4.79	4.88	0.47	0.47	0.47



**Table S9.** Hydrogen bond network time constants for hydrophobic cavities. Symbols and regions are as in Table S8.

	$\tau_R^{WW}$ (ps)	$\tau_R^{WW}$ ( $d > d_{int}$ ) (ps)	$\tau_R^{WW}$ ( $d < d_{int}$ ) (ps)	$\tau_{HB}^{WW}$ (ps)	$\tau_{HB}^{WW}$ ( $d > d_{int}$ ) (ps)	$\tau_{HB}^{WW}$ ( $d < d_{int}$ ) (ps)
Bulk	3.66	—	—	0.42	—	—
HC1	4.28	3.63	4.53	0.44	0.41	0.45
HC2	4.13	3.65	4.39	0.44	0.43	0.44
HC3	4.09	3.71	4.38	0.44	0.44	0.44
HC4	4.09	3.76	4.38	0.44	0.44	0.44
HC7.5	4.06	3.86	4.36	0.45	0.46	0.44
HC10	4.00	3.84	4.33	0.46	0.46	0.44

**Table S10.** Hydrogen bond network time constants for AOT RMs. Symbols and regions are as in Table S8.

	$\tau_R^{WW}$ (ps)	$\tau_R^{WW}$ ( $d > d_{int}$ ) (ps)	$\tau_R^{all}$ ( $1.5 < d < d_{int}$ ) (ps)	$\tau_R^{WW}$ ( $1.5 < d < d_{int}$ ) (ps)	$\tau_{HB}^{WW}$ (ps)	$\tau_{HB}^{WW}$ ( $d > d_{int}$ ) (ps)	$\tau_{HB}^{WW}$ ( $1.5 < d < d_{int}$ ) (ps)
Bulk	3.66	—	—	—	0.42	—	—
$w_0 = 1$ (AOT)	6.65	9.88	5.16	5.17	0.41	0.52	0.33
$w_0 = 2$ (AOT)	5.58	5.48	5.21	5.50	0.42	0.45	0.38
$w_0 = 3$ (AOT)	4.70	4.89	4.51	4.47	0.42	0.47	0.36
$w_0 = 4$ (AOT)	4.79	4.89	4.68	4.65	0.44	0.49	0.37
$w_0 = 7.5$ (AOT)	4.73	4.75	4.68	4.65	0.46	0.50	0.37
$w_0 = 10$ (AOT)	4.61	4.63	4.56	4.49	0.47	0.50	0.37

**Table S11.** Hydrogen bond exchange times for hydrophobic cavities.

	$\tau_{exch}^{WW}$ (ps)	$\tau_{exch}^{WW}$ ( $d > d_{int}$ ) (ps)	$\tau_{exch}^{WW}$ ( $d < d_{int}$ ) (ps)
Bulk	2.18	—	—
HC1	2.96	1.79	3.34
HC2	2.80	1.85	3.24
HC3	2.61	1.87	3.11
HC4	2.57	1.89	3.09
HC7.5	2.40	1.97	3.03
HC10	2.27	1.94	2.90

**Table S12.** Hydrogen bond exchange times for AOT RMs.

	$\tau_{exch}^{WW}$ (ps)	$\tau_{exch}^{WW}$ ( $d > d_{int}$ ) (ps)	$\tau_{exch}^{WW}$ ( $1.5 < d < d_{int}$ ) (ps)
Bulk	2.18	—	—
$w_0 = 1$ (AOT)	1.82	1.34	2.05
$w_0 = 2$ (AOT)	2.12	1.53	2.57
$w_0 = 3$ (AOT)	2.91	2.91	2.81
$w_0 = 4$ (AOT)	3.03	3.03	2.75
$w_0 = 7.5$ (AOT)	2.74	2.67	2.61
$w_0 = 10$ (AOT)	2.66	2.61	2.56

**Table S13.** Hydrogen bond exchange times for NI nanopores.

	$\tau_{exch}^{WW}$ (ps)	$\tau_{exch}^{WW}$ ( $d > d_{int}$ ) (ps)	$\tau_{exch}^{WW}$ ( $d < d_{int}$ ) (ps)
Bulk	2.18	—	—
$w_0 = 1$ (NI)	1.79	1.34	2.05
$w_0 = 2$ (NI)	2.12	1.53	2.57
$w_0 = 3$ (NI)	2.09	1.55	2.61
$w_0 = 4$ (NI)	2.25	1.66	2.86
$w_0 = 7.5$ (NI)	2.16	1.76	2.86
$w_0 = 10$ (NI)	2.16	1.84	2.85

## II. Supplementary Figures

Figures S1 and S2 show time correlation functions [orientational,  $C_{HB}(t)$ , and  $S_{HB}(t)$ ]. Figure S3 shows the molecular jump mechanism and average number of hydrogen bonds for bulk water. Figures S4 – S8 show the same information as Figure S3 for bulklike water in ionic RMs, interfacial and bulklike water in NI RMs, and interfacial and bulklike water in HCs.

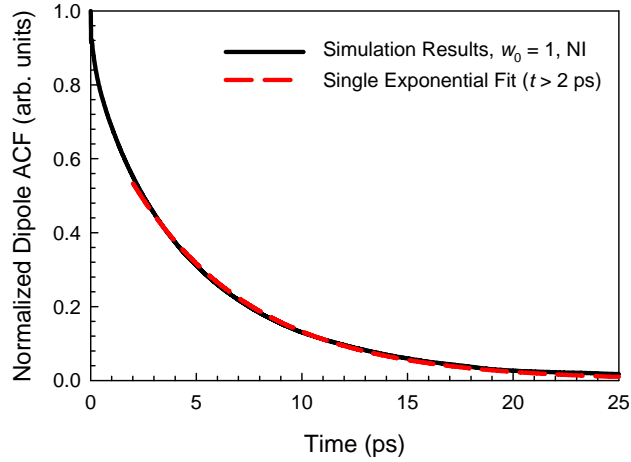


**Figure S1.** Normalized dipole autocorrelation function obtained from the simulation of nonionic reverse micelles with  $w_0 = 1$  (black solid line) and a single exponential fit at times longer than 2 ps (red dashed line). The ACF decays essentially exponentially at times greater than 2 ps.

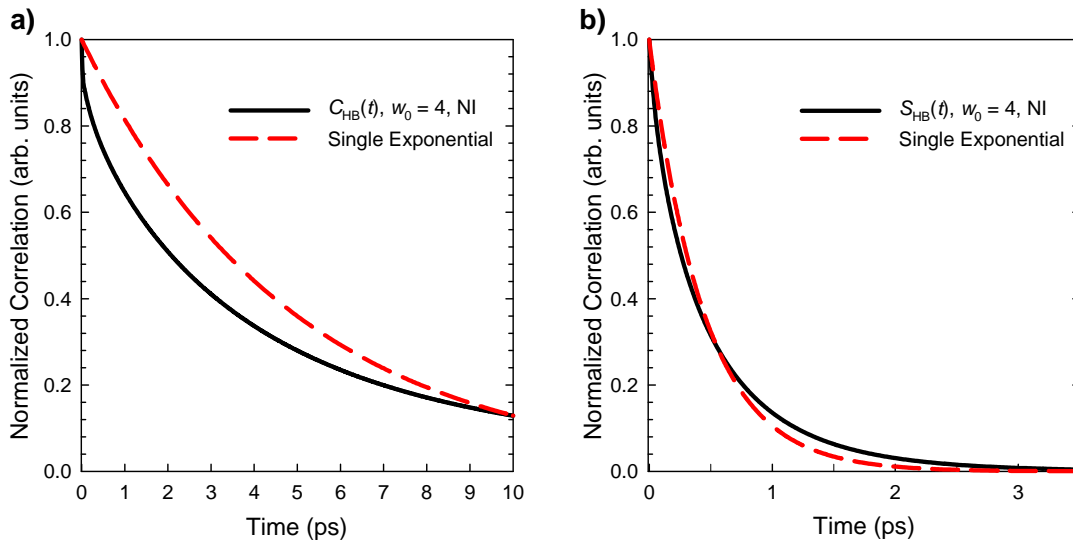


**Figure S2.** Comparison of  $C_{HB}(t)$  (part (a)) and  $S_{HB}(t)$  (part (b)) obtained from simulations and a single exponential decay (solid black and red dashed lines, respectively). It is seen that these quantities do not decay exponentially.



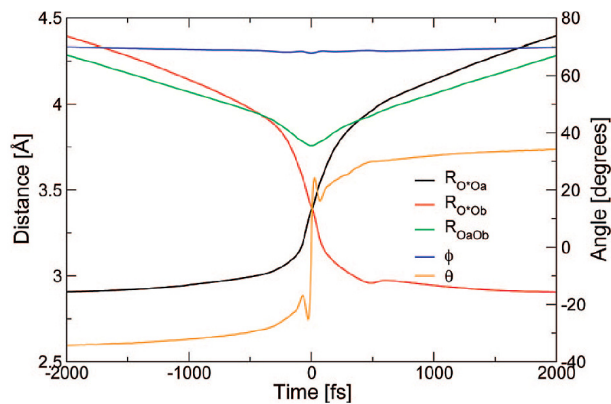


**Figure 3.** Average H-bond exchange trajectory: time-evolution of the geometric coordinates defined in Figure 2. The time origin  $t = 0$  is defined by  $\theta = 0$ .

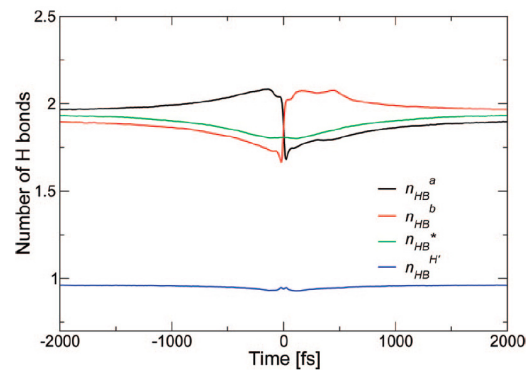


**Figure 4.** Average H-bond exchange trajectory: time-evolution of the H-bond coordination numbers. The  $n_{HB}^{ab*}$  are the number of H-bonds received by  $O^a$ ,  $O^b$ , and  $O^*$ , respectively, and  $n_{HB}^{H^*}$  is the number of H-bonds donated by  $O^*$  via its other hydrogen besides  $H^*$ .

**Figure S3.** Molecular jump mechanism and average number of hydrogen bonds in bulk water. Left side is Figure 3 from Laage, D. and Hynes, J. T., *J. Phys. Chem. B*, **2008**, *112*, 14230–14242. Right side is Figure 4 from same publication.

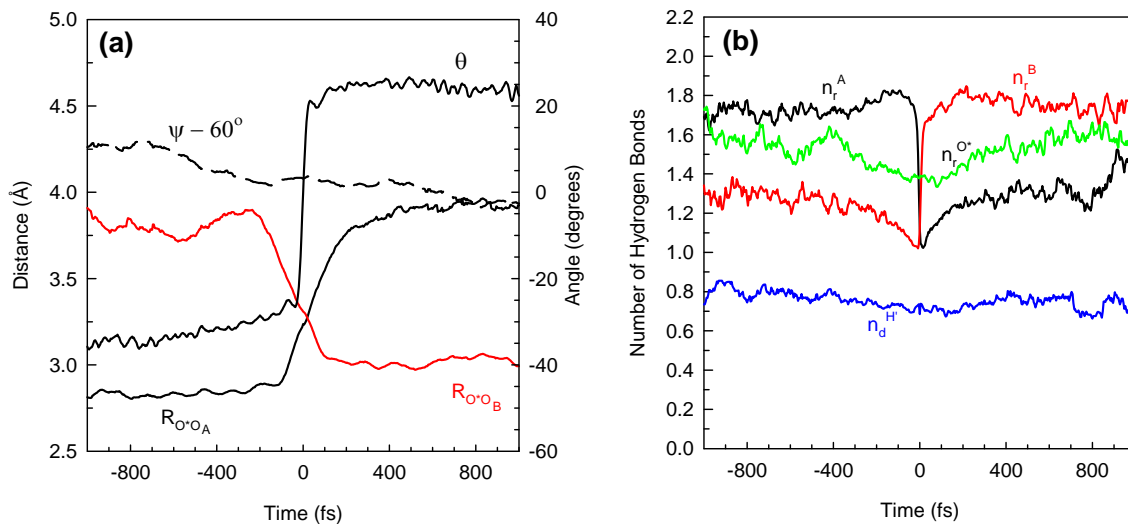


**Figure S4.** Molecular jump mechanism (a), and average number of hydrogen bonds (b) for bulklike water in ionic AOT RMs.

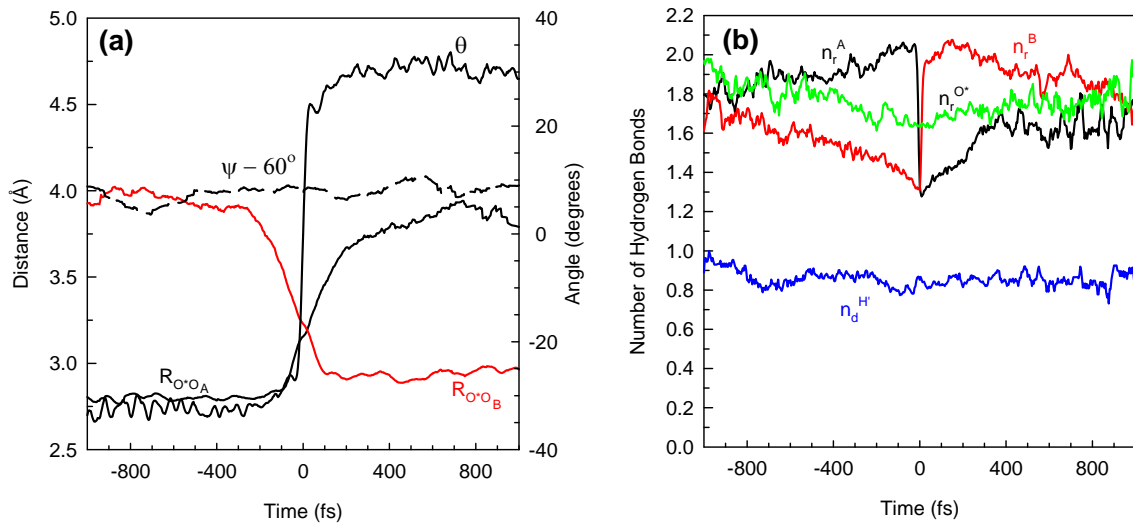


**Figure S5.** Same as Figure S4, but for interfacial water in NI RMs.

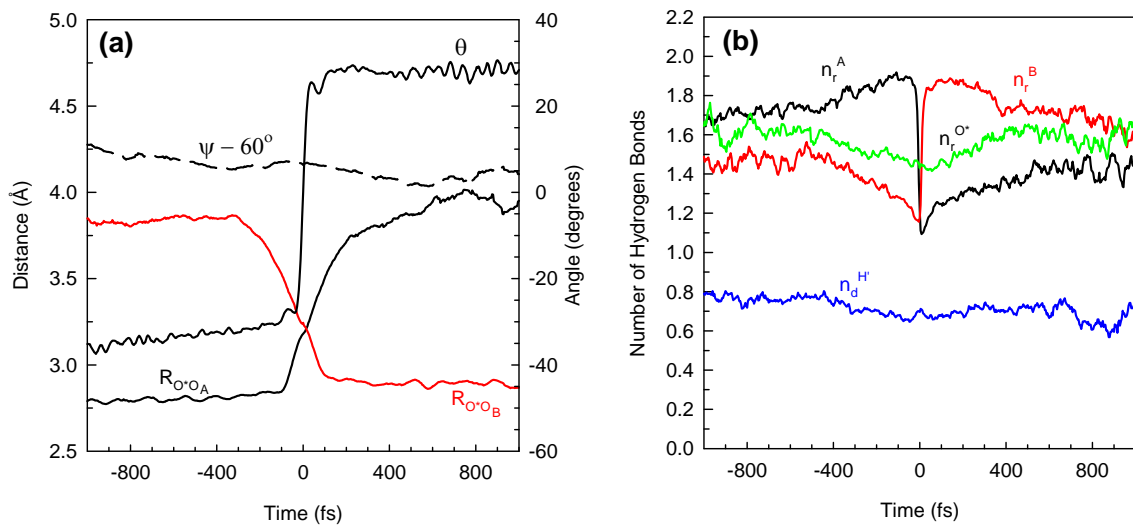


**Figure S6.** Same as Figure S4, but for bulklike water in NI RMs.

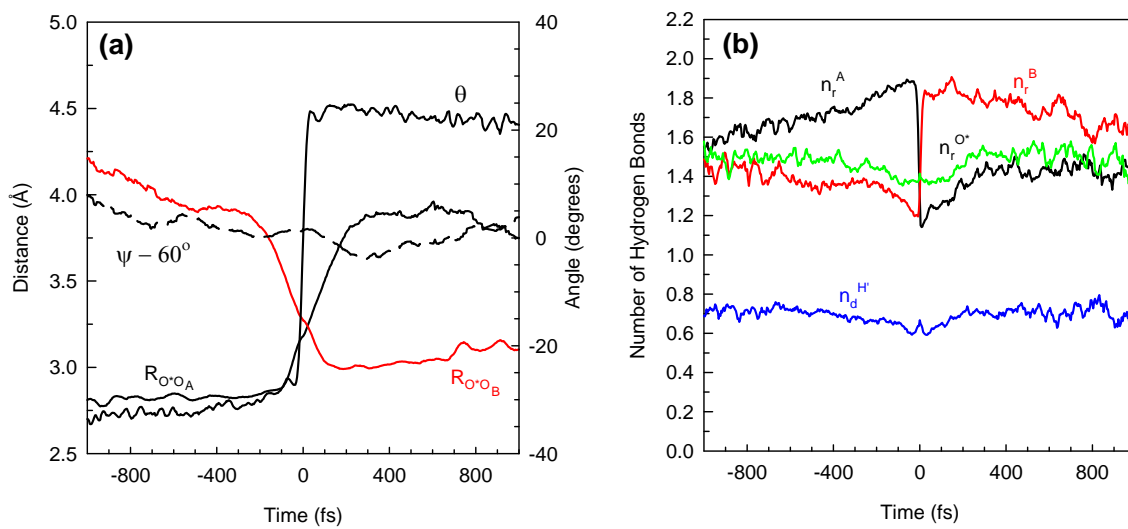


**Figure S7.** Same as Figure S4, but for interfacial water in HCs.

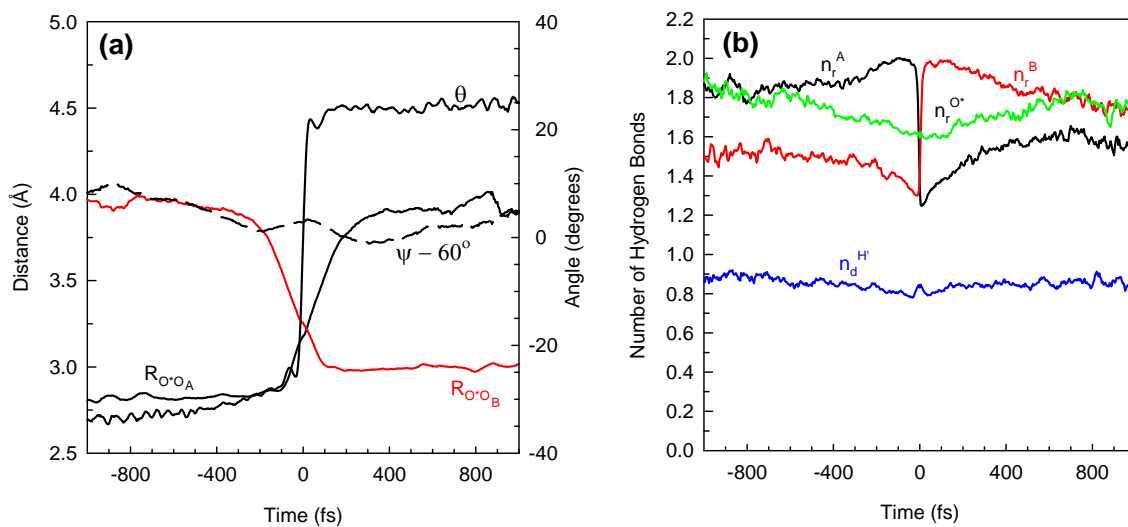


**Figure S8.** Same as Figure S4, but for bulklike water in HCs.